Published in final edited form as:

Lira, R. d., Robinson, T., Dimova, R., & Riske, K. A. (2019). Highly efficient protein-free fusion: a giant vesicle study. Biophysical Journal, 116(1), 79-91. doi:10.1016/j.bpj.2018.11.3128.

Highly efficient protein-free fusion: a giant vesicle study

R. B. Lira, T. Robinson, R. Dimova, K. A. Riske

Highly efficient protein-free fusion: a giant vesicle study

R. B. Lira[1,2], T. Robinson[1], R. Dimova[1,*] and K. A. Riske[2,*]

[1]Departamento de Biofísica, Universidade Federal de São Paulo, São Paulo, Brazil.
[2]Department of Theory and Bio-Systems, Max Planck Institute of Colloids and Interfaces, Potsdam, Germany.
*Address correspondence to: dimova@mpikg.mpg.de and kariske@unifesp.br

KEYWORDS: giant vesicles, fusion intermediate, confocal microscopy, vesicle electrodeformation, FRET, FLIM-FRET, microfluidics, POPG, DOTAP

ABSTRACT: Membrane fusion is a ubiquitous process in biology and is a prerequisite for many intracellular delivery protocols relying on the use of liposomes as drug carriers. Here, we investigate in detail the process of membrane fusion and the role of opposite charges in a protein-free lipid system based on cationic liposomes (LUVs) and anionic giant unilamellar vesicles (GUVs) composed of different palmitoyloleoylphosphatidylcholine:palmitoyloleoylphosphatidylglycerol (POPC:POPG) molar ratios. By using a set of optical microscopy- and microfluidics-based methods, we show that liposomes strongly dock to GUVs of pure POPC or low POPG fraction (up to 10 mol%), in a process mainly associated with hemifusion and membrane tension increase, commonly leading to GUV rupture. On the other hand, docked LUVs quickly and very efficiently fuse with negative GUVs of POPG fractions at or above 20 mol%, resulting in dramatic GUV area increase in a charged-dependent manner. Importantly, both hemifusion and full fusion are leakage-free. Fusion efficiency is quantified by the lipid transfer from liposomes to GUVs upon fusion using fluorescence resonance energy transfer (FRET), which leads to consistent results when compared to fluorescence lifetime-based FRET. We develop an approach to deduce the final composition of single GUVs after fusion based on the FRET efficiency. We can conclude that fusion is driven by membrane charge and appears to proceed up to charge-neutralization of the acceptor GUV.

INTRODUCTION

Membrane fusion is a ubiquitous process in biology, fundamental in events such as egg fertilization, viral infection as well as hormone and neurotransmitter release (1, 2). Membrane fusion follows successive steps including (i) docking of the opposing bilayers, (ii) membrane adhesion and lipid destabilization, (ii) fusion of the outer leaflets – termed hemifusion, (iv) fusion pore formation and expansion of the fusion neck and eventually (v) full fusion (1, 3). In the docked state, the opposing membranes are in direct physical contact but their bilayers are intact. The subsequent merging of the membranes outer

leaflets (hemifusion) results in mixing of lipids from both external monolayers, but the aqueous contents encapsulated by the membranes are still separated by a single bilayer. Eventually a small fusion pore opens and it may or may not expand (1-6). Full fusion is the result of complete pore expansion and merging of both aqueous compartments, yielding a final membrane with an additional equal to the sum of the areas of the otherwise separated membranes. In cells, membrane docking followed by lipid destabilization usually rely on a complex protein machinery, e.g. the SNARE proteins in synaptic vesicles and the viral fusion proteins in viral infection. Fusion can also be triggered by other (non-physiological) stimuli.

Studying membrane fusion *in vivo* is challenging because of its fast, dynamic and complex nature. For this reason, many *in vitro* systems have been developed in the last years (see e.g. Ref. (7)) to unravel the molecular requirements of fusion and, in some cases, its intermediates. In synthetic systems, a number of distinct fusogenic stimuli, such as reconstituted proteins (8, 9), electric pulses (10, 11), laser irradiation (12), and plasmonic and nano-heaters (13, 14), fusion peptides (15, 16) and polymers (17, 18), can mediate fusion, and it is assumed that most fusion events transit through the same fusion intermediates (except in the case of fusion induced by electromagnetic fields), even though they may differ in dynamics. Methods for detecting fusion and its intermediates usually rely on quenching or dequenching of fluorescent lipids present in the membrane, yielding a change in signal (decrease or increase, respectively) upon fusion (see e.g. Refs. (6, 19-21)). Lipid mixing is required but alone it is insufficient to assess complete fusion. In fact, extensive lipid mixing in instances of outer leaflet merging (hemifusion) or merging of the outer and inner monolayers can occur without simultaneous mixing of the internal bulk contents, possibly due to the formation of a small fusion pore which does not expand (22). Importantly, *in vitro* fusion is classically studied in populations of small or large liposomes (SUVs and LUVs, respectively) fluorescently labeled at self-quenching concentrations, and the measured changes in bulk fluorescence as used as the fusion readout (7, 19). In these assays, heterogeneities are hidden, information is averaged out and fusion intermediates are not easily or directly assessed – membrane docking and adhesion are not detected since there are no associated changes in fluorescence. In addition, it is often difficult to translate (de)quenching kinetics into useful quantitative data and results are prone to artifacts. Unequivocal assignment of docking, hemifusion and full fusion was accomplished with membrane-covered beads of two different sizes (16). However, content mixing and membrane morphological changes following fusion were not accessible due to the hard beads as membrane support. Furthermore, most protein-mediated fusion experiments require protein reconstitution in liposomes containing 10-30 mol% of charged lipids (23-27). Presumably, this fraction is empirically chosen, but it is not clear whether the charges are important for the protein environment, as a fusion mediator, or even, as recently reported, for vesicle docking (28).

In contrast to conventional liposome-based assays used to study membrane fusion, direct imaging of the fusion process using giant unilamellar vesicles (GUVs) (29) has the potential to unravel useful information not accessible in bulk assays. With the use of GUVs, mechanical parameters recognized to modulate or be modified during the fusion process are potentially accessible, including changes in membrane tension, curvature and elasticity as well as the molecular environment. Additionally, direct GUV observation potentially allows identification of fusion intermediates, detecting the area increase and elevated probe concentration in the fusion region (e.g. in self-quenched membranes). Surprisingly, despite these advantages, not many studies report the use of GUVs in investigating processes associated with membrane fusion. These relatively few studies include the first direct visualization of a peptide-induced fusion (30) and formation of a hemifusion diaphragm (31), heated nanoparticle-mediated fusion (32), resolving the very fast nature of the fusion neck expansion on the order of cm/s, (10) with rates depending on membrane properties (33), the role of regulatory proteins on SNARE-mediated fusion (34), charge (35) and multivalent ions (36), tension (37) and pH (38).

In this work, we introduce a protein-free GUV-LUV fusion system based on membranes of opposite charge and use a set of optical and mechanical methods for detailed investigation of the charge dependence of membrane fusion in a pure lipidic system. GUVs and LUVs closely mimic the curvature of the plasma membrane and fusion vesicles, respectively. The system offers the additional advantage that fusion can be directly observed between freely diffusing LUVs and individual relatively immobile GUVs. To study the effects of membrane charge, we use cationic LUVs of a fixed composition and GUVs as a model cellular membrane with increasing (negative) charge density in the membrane by changing the ratio of charged lipids over zwitterionic lipids. For the cationic LUVs, we took inspiration from a lipid mixture containing a fluorescent lipid analogue, which was demonstrated to quickly and spontaneously fuse with a number of cell lines, including those recognized to be difficult to transfect (39, 40). This interaction has proven effective for the intracellular delivery of materials to which the cell membrane is otherwise impermeable (41, 42). Importantly, these fusogenic liposomes constitute a promising carrier system, because they are able to fuse with the plasma membrane, and thus efficiently deliver the encapsulated cargo to the cytosol, and therefore circumvent the usual low efficient endocytic routes of conventional liposomes. The method described here is based on real-time imaging and manipulation of GUVs upon fusion with LUVs. In particular, quantification of lipid mixing is achieved by evaluating the intensity- and lifetime-based fluorescence resonance energy transfer (FRET) efficiency between the acceptor dye present in the LUVs upon fusion with GUVs containing the donor dye. FRET values are translated to fusion efficiency and measured on individual single GUVs with increasing fractions of negative lipids. In combination with lipid dye quenching, vesicle electrodeformation, and vesicle mixing in a microfluidic

device, we investigate how the membrane charge density on the GUVs controls the fusion efficiency, and whether fusion proceeds leakage-free.

MATERIALS AND METHODS

The phospholipids 1-palmitoyl-2-oleoyl-sn-glycero-3-phosphocholine (POPC), 1-palmitoyl-2-oleoyl-sn-glycero-3-phospho-(1'-rac-glycerol), sodium salt (POPG), 1,2-dioleoyl-sn-glycero-3-phosphoethanolamine (DOPE), 1,2-dioleoyl-3-trimethylammonium-propane (DOTAP), the fluorescent dyes 1,2-dipalmitoyl-sn-glycero-3-phosphoethanolamine-N-(lissamine rhodamine B sulfonyl) (ammonium salt) (DPPE-Rh), the head-group labeled 1,2-dipalmitoyl-sn-glycero-3-phosphoethanolamine-N-(7-nitro-2-1,3-benzoxadiazol-4-yl) (ammonium salt) (DPPE-NBD) were purchased from Avanti Polar Lipids (Alabaster, AL). Lipid solutions were prepared in chloroform in stored at -20°C until use. Sulforhodamine B (SRB), sodium chloride (NaCl), magnesium chloride (MgCl2), sucrose, glucose and sodium dithionite were purchased from Sigma Aldrich (St. Louis, MO) and used as received. Low-melting temperature agarose was purchased from Fisher scientific (Waltham, MA).

GUVs were formed by the electroformation method with little modifications (43), see Supporting Material Section S1. The vesicles were used fresh (the same day), thus for vesicles made of POPC and POPG mixtures, slightly higher PG concentration on the vesicle surface may be expected (44). Alternatively, the gel-assisted method (45) was used for GUVs with 100 mol% POPG. LUVs were produced by the extrusion method (41) For 3D imaging, GUVs were immobilized in agarose 0.1% (w/v) (43). To quantify area increase upon fusion, GUVs were placed on an electrofusion chamber (46) and connected to a function generator. For FRET imaging, vesicles were imaged with confocal microscopy in the sequential mode to minimize cross-talk for donor and acceptor excitation, Supporting Material Section S5. NBD-PE donor and DPPE-Rh acceptor fluorescence were detected upon donor excitation. FRET was also followed using a microfluidic device, see Supporting Material Section S4. GUVs were trapped in a PDMS-assembled chamber and solutions and LUVs were flushed through the microchannels at 2 μL/min. To distinguish hemifusion from full fusion, NBD-transferred to GUVs was quenched with dithionite, added to the GUV-LUV mix in the presence of SRB, Supporting Material Section S7. For FLIM (Supporting Material Section S11), the FRET donor NBD-DPPE was excited by a pulsed diode laser with a 40 MHz repetition rate in the presence or absence or the FRET acceptor.

RESULTS

We employed protein-free fusogenic liposomes (LUVs composed of DOTAP:DOPE:dye, 1:1:0.1) (39, 40) and GUVs primarily consisting of POPC with increasing molar fractions of POPG as a model of liposome-cell membrane fusion mediated by electrostatic interactions. Since the fusogenic liposomes already contain a lipid dye, they can be easily detected with fluorescence microscopy. Most of the results were obtained with LUVs labeled with DPPE-Rh (red; acceptor) as the fluorescent lipid dye and GUVs containing traces of NBD-PE (green; donor), because these fluorophores form a donor-acceptor FRET pair. Direct observation of GUVs enables detection of a number of distinct fusion intermediates such as membrane docking, hemifusion and full fusion, as deduced from the morphological response of the GUVs and the fusion efficiency assessed from the measured FRET signal, see Figure 1. In case of docking-only, the LUVs adhere to the GUVs which may be deformed due to the strong electrostatic interactions, but there is no or small associated FRET signal (Figure 1A,B). Upon hemifusion, the outer leaflet of GUVs contains the red dye from the hemifused LUVs, which can lead to a change in color of the GUV, and a low but detectable increase in FRET (Figure 1C); hemifusion can be also confirmed with quenching studies as we will see further. Upon full fusion of the outer and inner leaflets of the two vesicles, a large amount of LUV lipids are transferred to the GUV increasing its area, and the associated changes in FRET are significantly higher due to the large transfer of the acceptor dye (Figure 1D). Because both LUV and GUV compositions (and their dye fractions) are known before fusion, the FRET signal can be quantitatively translated into fusion efficiency and the membrane composition after fusion can be determined at the single-GUV level as demonstrated below.

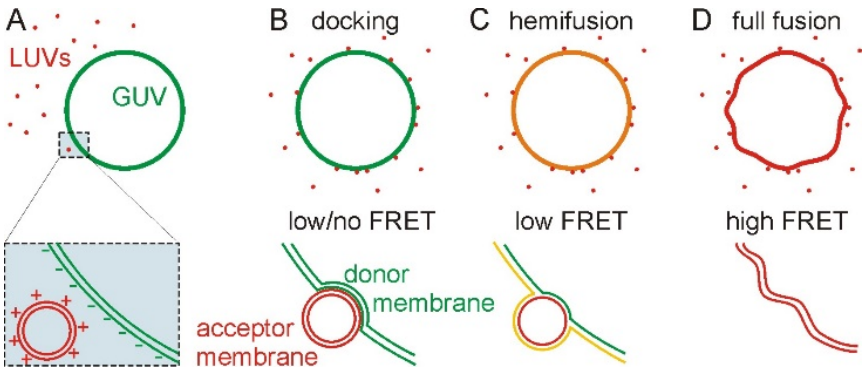

Figure 1. GUV-LUV fusion with associated observations of GUV morphology and FRET signal and their tentative interpretation. (A) GUVs containing the FRET donor (green) are incubated with fusogenic LUVs containing the FRET acceptor (red). (B-D) Schematics of the morphological and fluorescence changes accompanying the different fusion intermediates as directly observed under the microscope (upper row) and the associated leaflet rearrangement and FRET between the interacting pair for the respective intermediate (lower row). Fusion efficiency can be assessed from the measured FRET signal.

Interaction of fusogenic LUVs with neutral and negative GUVs. Fusogenic LUVs (30 μM lipid concentration) were incubated for 10-20 minutes with neutral POPC GUVs or negatively charged GUVs containing equimolar mixtures of POPC and POPG (the anionic fraction was chosen to approximately match the molar fraction of cationic lipids in the LUVs). Throughout the work, these GUVs are referred to as neutral and negative, respectively, unless mentioned otherwise. In the examples given below, we often make use of a protocol for GUV immobilization in 0.1-0.5 wt% agarose (43) to arrest the system for imaging and detect the fusion state (intermediates). The approach is based on building a "cage" around the GUV which stops its displacement, allowing for detailed 3D imaging, but leaves membrane fluctuations nearly unperturbed.

In samples of neutral GUVs, the LUVs appear stably docked to the membrane (adhered and diffusing across the GUV surface but not undocking), Figure 2A. Low but detectable amount of lipid transfer is also observed, see Section S2 in the Supporting Material. The LUVs are not visible in the NBD channel (Fig. S1) and therefore bleed-through is minimal, which is important for analyzing the FRET signal. The immobilization protocol was also used to very roughly quantify the number of docked LUVs on a single GUV, see Supporting Material Section S3. On the average, we found approximately 1 stably docked LUV per ~ 5 μm^2 of GUV surface. Interestingly, in a process similar to endocytosis, LUVs are often internalized into inward buds of neutral GUVs, in particular in vesicles exhibiting some excess area, Figure 2B, indicating possible changes in the GUV spontaneous curvature towards negative values (47). This can result from changes in membrane composition induced by asymmetric transfer of lipids (i.e. via hemifusion) and/or by LUV adhesion and engulfment coupled to membrane condensing effects by the charges on the LUVs. Although certainly interesting, the endocytosis-like process is out of the scope of this work.

In a striking contrast to neutral GUVs, incubation of LUVs with negative GUVs results in a massive transfer of lipids from LUVs to GUVs, as detected by the intense red fluorescence of the GUV surface (Figure 2C). The amount of transferred lipids is so high that the GUVs display large changes in their morphology, gaining a significant area stored in the form of membrane folds, buds and tubes as discussed below.

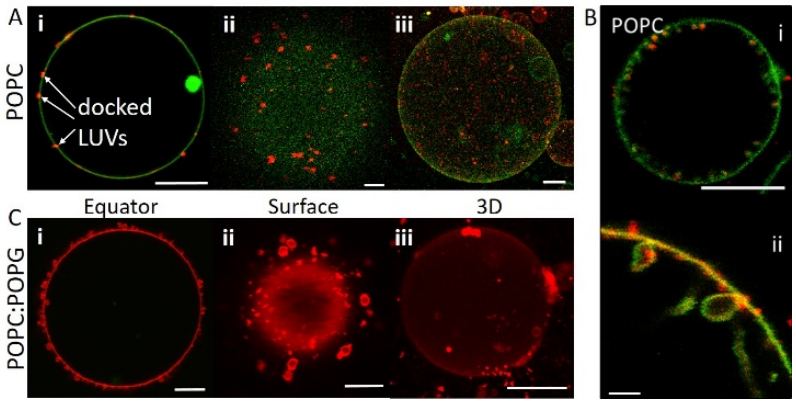

Figure 2. Different interactions of fusogenic LUVs with neutral (pure POPC) and negative (POPC:POPG 1:1) GUVs: (A) docking, (B) engulfment and (C) full fusion. Images in panels (A) and (C) represent (i) equatorial cross sections, (ii) GUV top surface, and (iii) three-dimensional reconstructions. In (A) and (B), the red dots correspond to docked LUVs and images are overlay of NBD and rhodamine (Rh) direct excitation and emission. In (B), neutral GUVs engulf fusogenic LUVs: (i) a whole vesicle and (ii) a zoomed-in region. In (C), images show directly the FRET channel signal (NBD excitation and Rh detection). Images were contrast-enhanced for better visualization (see also Fig. S1 for FRET signal from such vesicles). Vesicles were immobilized in agarose. Scale bars are 10 μm except in A(ii), B(ii) and C(ii) where they represent 2 μm.

Real-time observation of GUV-LUV interaction: membrane fusion increases GUV area. The results presented above were obtained after incubation of GUVs with the fusogenic LUVs and subsequent observation (imaging with and without GUV immobilization after incubation showed similar behavior). In order to reveal processes during the incubation, i.e., along the fusion pathway, we attempted to monitor in real time the interactions upon direct contact of the LUVs (30 μM lipids) and GUVs. This was performed in different ways, and the results are summarized in Figure 3. Initially, we observed the fusion process on negative GUVs trapped into a microfluidic chip, where the external solution could be exchanged almost instantaneously (~400 ms, see Section S4 and Movie S1 in the Supporting Material) using a technology developed previously (48, 49). Differently from other microfluidic technology for observing membrane fusion events (14, 50), here, we trapped single GUVs and fusion was initiated by operating an integrated valve to controllably add a specific concentration of LUVs (see Supporting Material Section S4 for details Our results obtained on-chip suggest that fusion is fast, as shown in Figure 3A. Already in the first 30 s a significant decrease in NBD fluorescence due to FRET. Structures inside the GUV remain inaccessible (green) to the LUVs. The relative FRET efficiency (E_{FRET}) was measured according to $E_{FRET} = I_{Rh}/(I_{Rh} + I_{NBD})$ where I_{Rh} and I_{NBD} are the respective Rh and NBD fluorescence intensities when only NBD is excited (51), see Supporting Material Section S5. Already in the first ~100 s, E_{FRET} is observed to reach a plateau approaching 1 (right panel in Figure 3A), which may result either from saturation of the fusion process or/and because of the definition of this quantity (for $I_{Rh} \gg I_{NBD}$, E_{FRET} approaches 1 by default).

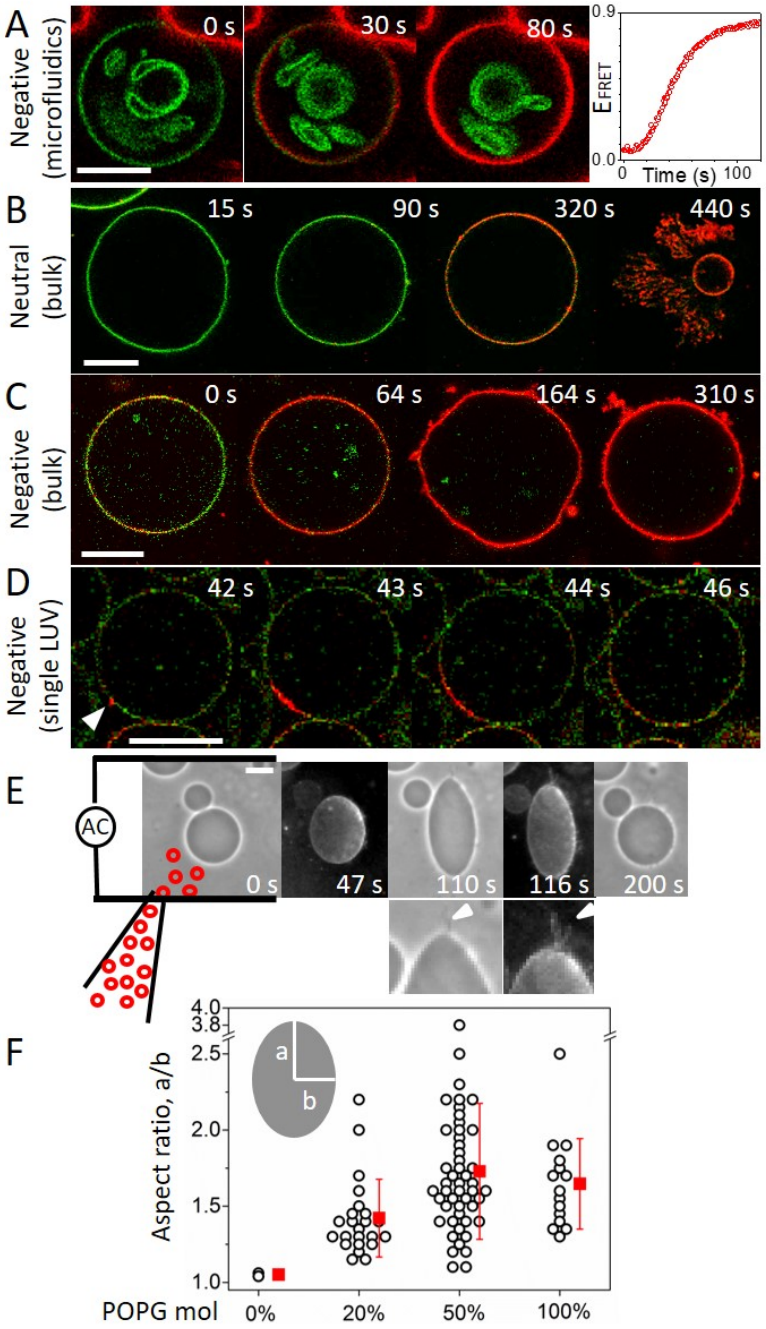

Figure 3. GUV morphological transformations observed in real-time upon addition of LUVs. (A-D) Confocal images of a neutral and negative GUVs either trapped in a microfluidic device (A) or free floating in the bulk (B-D). Images are overlay of NBD and Rh direct excitation and emission. In (A), the external solution was fully exchanged with LUVs (30 μM lipids) already in the first 400 ms. The NBD signal decreased and the FRET increased approaching 1 after ~100 s (figure on the right), while the internal structures in the GUV retain their green (NBD) intensity as they are not exposed to the LUV solution. The sequences (A-C) are shown in Movies S1 and S3 in the Supporting Material. (D) A single LUV fusion event (acquisition was performed at higher frame rate resulting in lower signal-to-noise ratio). The time stamps in (B-D) indicate the time after initiating the observation on each vesicle. The arrowhead at 42 s in (D) points to the initially docked LUV which becomes brighter as the partially self-quenched dye dequenches upon fusion, followed by a decrease as the dye is diluted. (E) Phase contrast and epifluorescence images of electrodeformation of a negative non-labeled GUV under an AC field (100 V/cm, 100 kHz).

The local injection of a concentrated LUV suspension (red circles) is schematically represented in the first snapshot. Zoomed regions below show formed lipid tubes (arrowheads). The timestamps show time after LUVs are introduced in the chamber. The sequence is shown in the Movie S4. All scale bars: 20 μm. (F) Maximum aspect ratio a/b (as sketched in the inset) of electrodeformed GUVs upon LUV injection to final bulk concentration of 42 nM. Each point indicates a single measurement on an individual GUV. Mean average and standard deviations are also indicated (red).

The microfluidic chip geometry and the flow applied to exchange the solution around the GUVs did not allow us to follow the associated morphological changes. We thus performed experiments, in which a concentrated suspension of LUVs (30 μM final lipid concentration after equilibration) was locally introduced in one corner of the observation chamber. The LUVs reach the GUVs by diffusion. Although kinetic information cannot be extracted in this experiment, as LUV concentration close to a GUV at a given time cannot be precisely estimated, we could monitor the process from the beginning until equilibration (52). Figure 3B,C shows respective sequences for a neutral and a negative GUV in the bulk interacting with LUVs. The starting times of the observations as indicated in the snapshots (t = 0s) is 10 to 30 s after mixing (note that vesicles located farther away from the place of LUV injection respond later). Initially, the neutral GUV is homogeneously fluorescent (green) and exhibits shape fluctuations, indicating that the vesicle is tensionless (Figure 3B, 15 s). As LUVs dock, the GUV changes its color and its membrane fluctuations are suppressed (90 s) due to an increase in membrane tension (the volume remains constant as fusion proceeds without leakage as discussed further below). Presumably, the vesicle excess area is consumed in the engulfment and wrapping of LUVs (see Figure 2B) as well as generating structures favoring negative spontaneous curvature (inward buds). Further docking (red spots visible on the GUV cross section at 320 s) results in additional tension and eventual vesicle rupture (440 s); note that the locally injected LUV concentration explored here is usually higher than that in the incubation experiments described above which presumably causes the rupture. Similar behavior was observed with GUVs with low fraction of POPG (5 mol%). The vesicle bursting does not result from adhesion to the glass potentially mediated by LUVs as the GUV is observed to continually displace due to convection (see Movie S2 in the Supporting Material). The ruptured GUV restructures into a smaller vesicle containing nanotubes and buds dotted with red LUVs. We also observed LUV-mediated GUV-GUV adhesion and increase in tension, resulting in vesicle rupture (Figure S6 in the Supporting Material).

In sharp contrast, the interaction with the negative GUVs leads to a fast and efficient transfer of LUV lipids (Figure 3C) as already suggested by the microfluidic experiments: the GUV is initially green (0 s – some fusion had occurred already before imaging started) and quickly acquires a strong DPPE-Rh fluorescence (64 s). Note that the Rh fluorescence is homogeneous over the GUV surface as docking is immediately followed by fusion. Further arrival of LUVs increases the vesicle fluctuation indicating area gained by fusion (164 s). Eventually, the GUV returns to its quasi-spherical geometry and the gained area

is stored in the form of outward membrane folds, buds and tubes (qualitatively similar formation of curved structures was previously observed upon fusion of a pair of GUVs (35)).

Interestingly, single fusion events can be also detected. Figure 3D shows a single LUV initially binding to and subsequently fusing with a negative GUV. At the dye concentration used (~4.76 mol%), Rh fluorescence is partially self-quenched in the LUV. Thus, the single fusion events are characterized by a local increase in fluorescence resulting from initial lipid dilution (self-quenching is lost), followed by a decrease in fluorescence as the LUV lipids diffuse away from the fusion point and get diluted into the GUV membrane.

Morphologically, neutral GUVs which do not rupture are tense and spherical with many surface-docked LUVs and exhibit low to intermediate changes in color, whereas negative GUVs initially show large fluctuations as a result of area acquired from fusion with the LUVs, and then gradually produce many membrane folds. In order to quantify the increase in area upon fusion, GUV-LUV interaction and fusion were followed in the presence of an AC electrical field. AC fields can be used to deform GUVs (53, 54) and to assess changes in area (53-56), which can be translated into the amount of transferred lipids (i.e. upon fusion). We applied AC field to initially spherical (little or no excess area) non-labeled GUVs and after the vesicle adopted its equilibrium shape as a result of electrodeformation, with a pipette we locally injected labeled LUVs (0 s). The POPG molar ratio in the GUVs was varied. Because at low POPG fractions LUVs tend to disrupt the GUVs in the presence of the electric field, the final LUV concentration was decreased to 42 nM. The LUVs diffuse to the GUV, which starts to elongate (in the direction of the field) into a prolate shape (57). A typical sequence is shown in Figure 3E. The onset of deformation coincides with the appearance of Rh fluorescence in the GUV membrane (47 s), as deformation is coupled with fusion. Deformation proceeds up to a maximum (92 s for this particular GUV), after which the vesicle starts to emit membrane projections (tubes) at the vesicle poles facing the electrodes (110 s), easily observed by fluorescence (116 s – see insets in Figure 3D). Afterwards, the vesicle returns to its quasi-spherical shape (200 s), and the acquired area is stored in external buds and tubes. Importantly, the vesicle optical contrast due to the sugar asymmetry is preserved, indicating that the fusion process is not accompanied by changes in membrane permeability, i.e. it is leakage free.

The area gained from LUV fusion is not completely used for GUV deformation under an electric field (i.e. tube formation). Thus, we simply measured the maximum attained aspect ratio a/b; see Figure 3F. Interaction of LUVs with neutral GUVs builds up tension in the membrane, leading to vesicle rupture. The very few GUVs that survived electrodeformation exhibited a negligible increase of the aspect ratio ($a/b \sim 1$). In contrast, significant deformation occurs for vesicles containing POPG at or above 20 mol%. The increase levels out at 50 mol%.

Full fusion vs. hemifusion assay: both are leakage-free processes. Whereas the morphological data presented above clearly demonstrate full fusion as the outcome of LUV interaction with GUVs at intermediate to high POPG fraction (≥ 20 mol%), the data presented so far is inconclusive as to the pathway for GUVs at lower POPG fraction. Indeed, our data (showing a large number of docked LUVs, small but significant lipid transfer from docked LUVs, increase in membrane tension and rupture) suggest that the process involves hemifusion, even though simple docking/adhesion with a low degree of full fusion cannot be ruled out. Distinguishing hemifusion (or even docking) from full fusion has proven to be a difficult task in both reconstituted and *in vivo* systems (25, 58, 59). Here, we take advantage of the fact that fluorescent dyes can be permanently quenched by specific molecules. In the presence of a membrane impermeable quencher added externally to the GUVs, membrane fluorescence acquired from dye-labeled LUVs should be completely quenched when the dye is located exclusively in the outer GUV leaflet, whereas quenching should be on the order of 50% when the dye is symmetrically present in both leaflets. Here, we used the well-known quenching agent sodium dithionite (herein referred to as dithionite) (60) for the selective quenching of NDB transferred from the LUVs to non-labeled GUVs, see also Ref. (61) for dithionite permeability. Control experiments with NBD-labeled GUVs show that dithionite quenches ~ 50% of the membrane fluorescence intensity (Section S7 and Figure S7), corresponding to quenching exclusively the membrane outer leaflet. As hemifusion of labeled LUVs with non-labeled GUVs should transfer the dye only to the external GUV leaflet, we expect quenching to reduce the fluorescence by significantly more than 50 % (the inner GUV leaflet would remain inaccessible to the quencher), as shown in control measurements (Figure S8). If full fusion is the only pathway, ideally, only ~50 % quenching is expected.

In the presence of LUVs, a small fraction of the GUVs (~23% for neutral and ~11% for negative vesicles) was observed to leak after the addition of dithionite. Thus, quenching experiments were carried out in the presence of the water-soluble dye sulforhodamine B (SRB) which was used to detect and exclude vesicles with compromised membrane where quenching of NBD in the internal leaflet could occur via dithionite permeation. Figure 4A shows images of neutral and negative, initially non-labeled GUVs incubated with DPPE-NBD-labeled LUVs. Incubation of neutral GUVs results in LUV docking and minor but detectable lipid (NBD) transfer, whereas incubation of negative GUVs results in significant and homogeneous lipid transfer (Figure 4A, upper panel) as shown above (Figures 2 and 3). When GUV-LUV incubation was performed in the presence of 10 mM of dithionite, NBD fluorescence from neutral GUVs is almost completely suppressed, whereas negative GUVs are still fluorescent; the data for a large number of GUVs is shown in Figure 4B. The results show that NBD is transferred exclusively via hemifusion to

neutral membranes and via full fusion to negative membranes. Importantly, in both cases, the GUV integrity upon fusion is preserved as SRB does not leak in, which is consistent with the preserved sucrose/glucose contrast as observed in Figure 3E. Note that for negative GUVs in the presence of dithionite, the membrane average fluorescence is still higher than 50% of the initial fluorescence. This signal could result from: (i) docked LUVs whose inner leaflets are inaccessible to dithionite, however, LUVs would be still visible as diffraction limited spots, which we did not observe; or (ii) dithionite concentration being insufficiently high to quench all outer NBD massively transferred upon fusion and hemifusion. Unfortunately, higher dithionite concentrations could not be employed because the GUVs became leaky (Figure S9). To summarize, the quenching experiments show that LUVs undergo docking and hemifusion with neutral GUVs and predominantly full fusion with negative GUVs, in agreement with the observed GUV area increase (Figure 3).

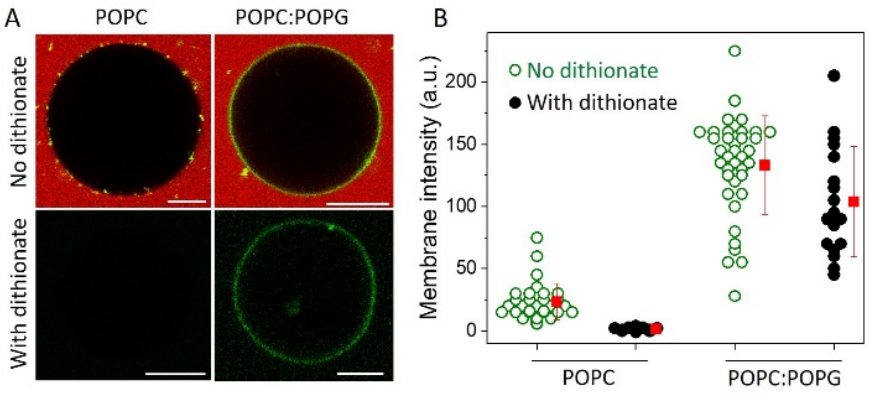

Figure 4. Quenching of NBD upon membrane fusion. (A) Non-labeled GUVs incubated with 1 μM NBD-labeled LUVs in the absence (upper row) and presence of 10 mM dithionite (lower row). Measurements were performed in the presence of 12.5 μM SRB (red). Images are overlay of NBD and SRB direct excitation and emission. For clarity, only membrane fluorescence is shown upon incubation with dithionite (lower row). Scale bars: 10 μm. (B) NBD fluorescence intensity for all tested conditions. Each point represents a measurement on a single non-permeable GUV. Mean average and standard deviations are also indicated (red).

A FRET-based single GUV assay: assessing the membrane composition upon fusion. The LUV-GUV interaction was observed to depend on the fraction of the anionic POPG lipid in the GUVs (see Figure 3F). We speculated that the GUV surface charge controls not only the affinity to the LUV membranes but also determines whether interacting vesicles undergo docking/hemifusion or full fusion as suggested by the quenching experiments. To unravel the role of membrane charge, we quantified the fusion efficiency for varying fractions of POPG in the GUVs. To this end, we developed a single GUV-based FRET assay using DPPE-Rh-labeled LUVs and DPPE-NBD-labeled GUVs, see Supporting Material Section S5. Fusion results in transfer of DPPE-Rh from LUVs to GUVs, and therefore increases FRET efficiency. Lipid transfer can be detected via Rh emission through NBD excitation. To relate FRET to fusion efficiency and

to assess the compositional change in the GUVs resulting from fusion, we constructed a calibration curve based on FRET signal detected in POPC GUVs containing a fixed amount of NBD (0.5 mol%, as in the fusion experiments) and increasing concentration of Rh (0 – 5 mol%), see Section S5.2 and Figure S5. The FRET signal for the calibration curve did not appear to depend on the presence of charged lipid or salt (data not shown). Since absolute FRET efficiencies depend on different parameters sometimes difficult to measure (i.e. the dipole orientation of the donor emission and acceptor absorption), the data presented here are sensitive within the range of donor and acceptor dye ratios used in the calibration. The advantages of using a FRET-based assay over a single-dye assay (i.e. detecting the signal from labeled LUVs fusing to non-labeled GUVs) are manifold: the possibility to observe GUVs before (and after) fusion by fluorescence, improved sensitivity of FRET-based assays and the detection of fusion intermediates (i.e. distinguishing docking from hemi- or full fusion).

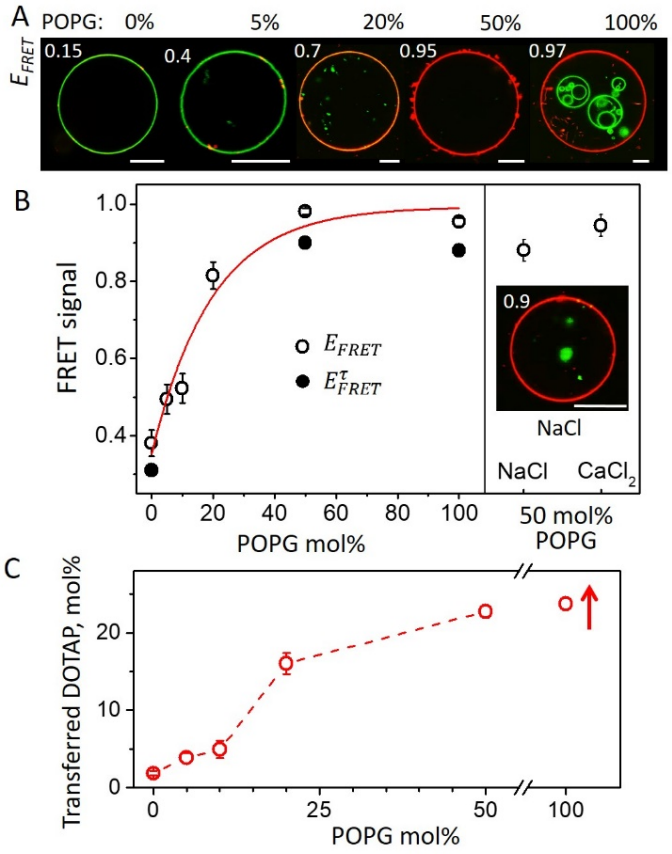

Figure 5. FRET-based assay for deducing the GUV membrane composition after fusion. (A) Confocal cross sections of different GUVs at increasing POPG molar fractions (indicated above each snapshot) incubated with LUVs (30 μM lipid). Images are overlays of NBD and Rh sequential direct excitation and emission and FRET channel, see Supporting Material Section S5. The respective E_{FRET} values are shown in the upper left corner. (B) Average intensity-based FRET, E_{FRET}, for GUVs of increasing POPG molar fractions (open circles); data from 25 to 40 GUVs per composition. The exponential fit (red curve) is a guide to the eye. FLIM-FRET data, E^{τ}_{FRET}, (solid circles) are included for comparison, see main text and Supporting Material section S11 for details. Right segment shows E_{FRET} measured for GUVs containing

50 mol% POPG in the presence of 100 mM NaCl or 5-50 mM $CaCl_2$. The inset shows one GUV in the presence of NaCl with E_{FRET} value indicated on the image. Scale bars: 10 μm. (C) Fraction of DOTAP in the GUVs after fusion for increasing POPG molar fraction in the membrane as deduced from the E_{FRET} values, see text. Upward arrow indicates possible underestimation of the measured parameters for 100 mol% POPG GUVs, see text for details. Error bars in (B, C) indicate standard errors.

Results from the incubation of LUVs with GUVs of increasing POPG mol% are shown in Figure 5A, with the respective measured E_{FRET} values. Note that being initially green, the GUVs display more DPPE-Rh fluorescence for increasing POPG mol%. Importantly, fusion is restricted to the bilayers in contact, as vesicles inside GUVs are protected from interaction and fusion with LUVs (see Figure 3A and the GUV image for POPG 100 mol% in Figure 5A). E_{FRET} values measured on a number of GUVs of different compositions are shown in Figure 5B. At low POPG fraction (≤ 10 mol%), E_{FRET} is low (0.35 – 0.5) and many LUVs are observed on the GUV surface (diffraction limited spots) suggesting hemifusion and docking. Increasing POPG to 20 mol% results in a two-fold increase in E_{FRET}. Deformation data (Figure 3) shows that at this fraction, interaction results in full fusion. Therefore, transition from mainly hemifusion to (predominantly) full-fusion occurs between 10-20 mol% POPG. Standard error rather than standard deviation is shown for clarity due to the large scatter at low POPG fractions, which could result from compositional heterogeneity of the prepared GUVs (62) and other factors discussed in more details in Supporting Material Section S8. Increasing POPG to 50 mol% and above results in further increase and saturation of E_{FRET} (~1). This could be interpreted as a result of charge compensation as the amount of cationic DOTAP transferred to GUVs via fusion equals the amount of anionic POPG and fusion no longer proceeds. However, we suspect that saturation in E_{FRET} also arises because, by definition, this quantity approaches 1 for $I_{Rh} \gg I_{NBD}$. In any case, data are less scattered at high POPG fractions also because the electrostatic interaction is more pronounced. Variations in the FRET signal can only be detected because individual GUVs are probed (see Supporting Material Figure S10), and this is in sharp contrast with bulk assays in which only average values are gathered, potentially including signal from ruptured membranes.

The driving force of fusion in the system is clearly of electrostatic nature. Therefore, it is plausible that fusion might be influenced by screening of the charges by salt. We incubated LUVs and negative GUVs dispersed in salt solutions of monovalent (100 mM NaCl) or divalent (5-50 mM $CaCl_2$) ions. Osmotic imbalance from the added salts was circumvented by reducing sugar concentrations accordingly. In these conditions, vesicle aggregation and adhesion was observed and the vesicles exhibited surface defects and folds; we examined only non-adhering defect-free portions of the GUVs. In both cases, fusion was as efficient as in the pure sugar solution, as shown in Figure 5B (see Supporting Material Figure S11 for data from individual vesicles), with measured E_{FRET} close to 1. Although somewhat unexpected, these results are not completely surprising. Other charge-mediated membrane fusion assays have reported little or no

effects of a range of salts on fusion of charged membranes (63-65). For the conditions described here, electrostatic interactions between membranes of opposite charges are so strong that the presence of these ions was not able to affect fusion at a detectable level. Presumably, the effect of salt will be more pronounced for lower PG fractions in the GUV membrane, which we are currently exploring.

An important advantage of the FRET assay we have developed is that it allows us to assess the GUV final composition after fusion with LUVs. From the calibration curve (Supporting Material Figure S5) and the value of E_{FRET} measured on GUVs that have undergone fusion, we can deduce the resulting Rh/NBD dye ratio and thus assess how much LUV lipids have been transferred to the GUV. The NBD amount on the GUV is fixed for the various fractions of POPG, while the amount of transferred Rh is proportional to that of DOTAP from the fusing LUVs. Thus, the final GUV composition upon fusion can be directly estimated from the Rh/NBD dye ratio, calculations are detailed in Supporting Material Section S5.2. In Figure 5C, we show the final DOTAP fraction reached in the GUV membrane upon fusion. At low POPG fractions, where docking and hemifusion dominate, the amount of transferred DOTAP is small, below 5 mol%. However, for GUVs with 20 mol% POPG, the amount of transferred DOTAP increases significantly and levels out for GUVs with ≥50 mol% POPG. As fusion of LUVs results in dilution of the GUV lipids, for GUV initially containing 50 mol% POPG, the increase of DOTAP fraction to around 23 mol% (Figure 5C) would imply ~1:1 final ratio of positive to negative charges, i.e. neutralization. However, this saturation may be an artefact from the reduced sensitivity at E_{FRET} values approaching 1 (indicated with a red upward arrow in Figure 5C for 100% POPG); note that because of the definition of this quantity (as long as $I_{Rh} \gg I_{NBD}$, E_{FRET} approaches 1 by default), the sensitivity to transferred DOTAP is reduced.

To roughly test the validity of our assessment for the final GUV composition after fusion, we prepared vesicles with composition approximating the final predicted GUVs after fusion. Measurements of the diffusion coefficient of these mimetic systems were consistent with measurements on GUVs after fusion, see Supporting Material Section S12 corroborating our findings for the membrane composition of the fused vesicles.

FLIM-FRET measurements of GUV-LUV fusion. Intensity-based FRET measurements are prone to artefacts (66), including decreases in signals due to photo-bleaching or changes in dye concentrations. The latter of which, could affect the E_{FRET} calculations above if the donor dye is significantly diluted upon fusion. Therefore, we performed similar experiments on GUV-LUV fusion using fluorescence lifetime imaging microscopy (FLIM) and calculated the resulting FLIM-FRET efficiencies (E_{FRET}^{τ}). Measurements involving fluorescence lifetimes do not suffer from the above intensity-based issues and as the FRET efficiencies can be calculated directly, there is no need for a calibration curve. Here, the donor

DPPE-NBD lifetime (τ) was measured in the absence and presence of the acceptor DPPE-Rh, before (τ_{before}) and after (τ_{after}) fusion, respectively. We performed FLIM-FRET measurements for increasing POPG mol% as a further validation of the intensity-based FRET, see Supporting Material Section S11. Before fusion, the average lifetime of DPPE-NBD τ_{before} in POPC GUVs is 7.74 ns and slightly lower for negative GUVs (6.49 and 6.59 ns for vesicles containing respectively 50 and 100 mol% POPG). Upon fusion with LUVs, the dye lifetime decreases (due to FRET) in a manner that depends on GUV charge: whereas for the neutral POPC the decrease in lifetime is moderate (τ_{after} = 5.34 ns), it is strongly reduced for GUVs containing 50 and 100 mol% POPG (τ_{after} = 0.59 and 0.80 ns, respectively) due to very efficient FRET, as a result of significant fusion. All values are displayed in Supporting Material Table S2.

From the measured NBD membrane lifetimes before and after fusion, it is possible to calculate the absolute FRET efficiencies using $E^{\tau}_{FRET} = 1 - \tau_{after}/\tau_{before}$. The data are displayed in Figure 5B, see also Supporting Material Figure S14. Even though the E^{τ}_{FRET} values obtained from FLIM images are quantitative rather than the relative FRET values taken from the intensity-based approach, it is still not possible to draw further conclusions regarding charge neutralization with pure POPG GUVs. This is due to the limitations of measuring the very short fluorescence lifetimes of DPPE-NBD resulting from extremely efficient fusion. Nevertheless, the FLIM-FRET data strongly agree with data from intensity-based FRET, highlighting the robustness of the charge-mediated GUV-LUV fusion assay.

DISCUSSION AND CONCLUSION

We have developed a protein-free GUV-LUV fusion system based on the interaction of membranes of opposite charge. Quantitative GUV imaging and manipulation allowed determination of the charges that control the well-defined fusion intermediate transitions at the level of single vesicles. The way cationic fusogenic LUVs interact with GUVs is determined by the charge density of the GUV membrane, here controlled by the molar fraction of the anionic lipid POPG. At low POPG fraction, LUVs stably dock to the GUV surface and undergo diffusional mobility. Such interaction results in little but detectable lipid transfer via membrane hemifusion and asymmetric lipid transfer to GUVs, leading to increase in their membrane curvature and tension, eventually causing rupture. In sharp contrast, the number of stably docked LUVs is much lower for the negatively charged GUVs as docking is immediately followed by fusion to membranes with intermediate to high POPG molar fraction (≥ 20 mol%). This results in massive lipid transfer via full fusion leading to pronounced increase in vesicle area together with monolayer area asymmetry inherently present on the LUVs (as discussed below and illustrated in Figure 6) and an increase in spontaneous tension.

The induced membrane tension which is evident from reduced membrane fluctuations (in the absence of electric field) or acting against electrodeformation and decreasing the aspect ratio a/b (both shown in Figure 3) can be caused by two factors: (i) LUV adhesion in the case of neutral GUVs, and (ii) fusion in the case of the charged GUVs. In the first case, the GUV excess membrane (initially stored in fluctuations) is consumed by the adhering vesicles, which might get engulfed (Figure 2B), or by hemifusion. In the second case, because of the small size (~70 nm in radius as measured with dynamic light scattering, Supporting Material Section S1), the fusing LUVs are characterized by a difference in the areas of their membrane leaflets (the outer leaflet area is larger by ~5%). Upon hemifusion and full fusion, the leaflets of the GUVs increase asymmetrically in area (the outer leaflet acquiring more lipids) which induces a positive spontaneous curvature (67, 68), as schematically illustrated in Figure 6. This in turn leads to the generation of highly curved protrusions (nanotubes and buds) and an increase in the spontaneous tension (69, 70). As a result, the projected area of the vesicle decreases. In a similar system, an increase in GUV area upon fusion was observed followed by the formation of dense lipid aggregates at the GUV surface rather than membrane tubes (71).

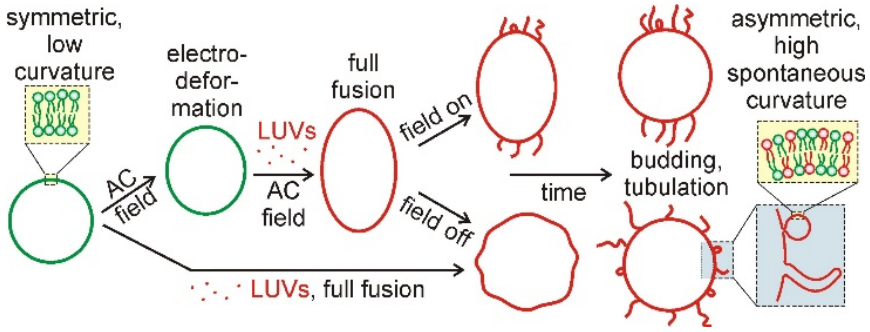

Figure 6. Morphological changes associated with changes in curvature upon full fusion. An initially flat GUV membrane has almost zero membrane (spontaneous) curvature, and is amenable to deformation under an AC field. An initial increase in vesicle area resulting from fusion with LUVs (red dots) is observed as an increase in GUV deformation under AC field (upper pathway) or as an increase in membrane fluctuations in the absence of AC field (lower path). In the former case, the curved structures are aligned with the field direction. The LUVs, inherently bearing a leaflet area asymmetry (more lipids are present in their outer leaflet), impart this asymmetry to the GUVs upon fusion. The GUV membrane acquires a higher fraction of LUV lipids on its external leaflet inducing positive spontaneous curvature which stabilizes highly-curved outward tubes and buds.

Under AC field, the produced tubular structures are located predominantly at the vesicle poles facing the electrodes, see Figures 3E and 6, compared to tubulation over the whole vesicle surface in the absence of the field, Figure 3C. This could be due to (i) the higher local curvature at the poles of the elliptical GUV facilitating the tube formation and (ii) field-induced accumulation of charged lipids in this

region, leading to locally enhanced fusion efficiency and increased spontaneous curvature. Similar behavior was observed recently on electrodeformed GUVs doped with light-responsive molecules (72).

The spontaneous curvature m resulting from the GUV membrane asymmetry acquired during fusion with the LUVs (Figure 6) acts to generate tension (spontaneous tension) ~ $2\kappa m^2$, where κ is the membrane bending rigidity (κ ~3.6×10^{-20} J as reported for membranes doped with PG (73)). Because the elliptical deformation as induced by the electric field is suppressed during fusion, we can assume that the generated spontaneous tension, which brings back the vesicle to a sphere, is higher than the electric-field tension. The latter can be roughly estimated from the vesicle shape (before the onset of fusion) and field amplitude (74) and in our experiments is on the order of 10^{-2} μN/m. This implies that the lower limit of the spontaneous tension is of similar magnitude. Thus, the corresponding spontaneous curvature induced during fusion is at least on the order of 1/(2.6 μm). This implies that the diameter of the produced buds and tubes is in the (sub)micron range (for small buds and necklace tubes, the spontaneous curvature is $m = 1/R_{sph}$ where R_{sph} is the radius of the spheres or the bud; for cylindrical tubes with radius R_{cyl}, $m = 0.5/R_{cyl}$). Indeed, the initial tubes that are observed protruding at the poles of the vesicles during electrodeformation (see Movie S4 and Figure 3E) have these diameters and seem to become thinner and with diameters not optically resolvable as fusion proceeds further. The exact change in the membrane spontaneous curvature can be assessed with tube-pulling experiments (70) or micropipette aspiration (75) and remains to be confirmed. Presumably, lipid flip-flop over time would allow for relaxing the spontaneous curvature acquired from fusion.

To measure fusion efficiency, we developed a quantitative FRET-based assay that enables measurements on a single-GUV level. Construction of a calibration curve with a controlled ratio of fluorescent donor and acceptor dyes allowed assessing the changes in membrane composition from measurements of intensity-based FRET (E_{FRET}) in fused GUVs. The fusion efficiency as assessed from intensity-based FRET was further validated with FLIM-FRET (E^{τ}_{FRET}). We showed that membrane charge is the driving force for fusion and controls the transition from docking/hemifusion to full fusion. In the high FRET regime, even though both intensity and lifetime-based FRET lose sensitivity (and the ability to determine membrane compositional changes), mechanical deformation of GUVs under an electrical field showed that the degree of deformation for pure POPG GUVs is similar to that of GUVs containing 50 mol% POPG. This may suggest saturation of the fusion process and that charges are only partially neutralized in pure POPG GUVs. However, GUV electrodeformation does not show the full area gain resulting from fusion because of the imposed spontaneous tension stemming from the acquired asymmetry between the membrane leaflets. As a consequence, the degree of deformation is a balance between fusion efficiency

(that favors deformation) and spontaneous tension (that suppresses deformation). Therefore, it remains unclear whether charges on pure POPG GUVs are also neutralized.

The charge-dependent fusion system described here recapitulates all fusion steps observed with protein-reconstituted systems (i.e. SNARE fusion), and the fusion efficiency is as high as or higher than most reconstituted systems described in the literature. For example, SNARE-only liposomes are shown to result simply in hemifusion, whereas full fusion requires additional regulatory proteins (76, 77). The dependence of the transition of fusion intermediates from docking to hemifusion as a function of POPG fraction is reminiscent of that in SNARE-reconstituted systems where transitions also depend on SNARE density (8). In terms of POPG molar fraction, hemifusion to full fusion occurs at 10-20 mol% POPG, and saturation occurs at 50 mol% POPG or above. These conditions result in final DOTAP fraction in the GUV from below 5% to near 25% after hemifusion and full-fusion, respectively. None of the results are influenced by mono- and di-valent ions such as Na^{+} and Ca^{+2}, and in contrast to other systems (78-80), both docking/hemifusion and full fusion are leakage-free. Moreover, fusion proceeds with kinetics faster than most SNARE systems even in the presence of regulatory proteins (21, 23, 25, 34, 76, 77, 81).

The GUV-LUV fusion system explored here does not allow for fully resolving the kinetics of (single) fusion events as is the case of systems employing membrane patches or supported bilayers using total internal reflectance fluorescence microscopy (82-84). However, our approach allows for distinguishing whether fusion proceeds leakage-free, overcomes effects associated with membrane tension and allows for assessing the area growth and associated curvature affects.

We observed a large variation in fusion efficiency among vesicles of a given composition, especially for low POPG fractions. This can result from (i) membrane compositional heterogeneity and (ii) variations in surface tension. Indeed, recent observations by us point to variations in the molar fraction of charged lipids among different electroformed GUVs (Lira *et al.*, unpublished data; see also Ref. (44)). This effect is negligible for high POPG mol%, where fusion is very efficient. However, it is very pronounced for lower POPG fractions (10-20 mol%) where transition from hemifusion to full fusion is observed. In addition, membrane tension varies by orders of magnitude among different vesicles in the same sample, from 10^{-9} – 10^{-3} N/m (46, 71, 85). Membrane tension is known to regulate fusion (37, 86, 87), and such large variations in tension among different GUVs certainly affects the fusion efficiency, especially at low POPG molar fractions.

The LUV membrane composition contains nearly 50 mol% of DOPE, a lipid with a preferred negative curvature and a tendency to form hexagonal phases (88). This explains the strong efficiency of PE-containing liposome formulations to fuse with cells and the associated higher drug/nucleotide delivery efficiency when compared to lipids with lamellar phase preference. The different effects of membrane

charge density and phase preference also controls the trafficking route of hexagonal/lamellar phase liposomes into cells (89). Switching the delivery route from endocytosis to direct fusion with the plasma membrane would increase both delivery speed and efficiency, circumventing the limiting barriers associated with intracellular trafficking and potentially decreasing transfection cytotoxicity. Direct fusion is indeed an efficient way to transfer materials of a wide range of sizes and physical-chemical properties directly into the cell cytosol (42). Importantly, the fact that the fusion efficiency is increased with anionic membranes could help target the enclosed therapeutic substances in fusogenic liposomes to tumor cells, which expose a significant fraction of the anionic lipid phosphatidylserine. Understanding the role of membrane charge density and how it controls the transition of fusion intermediates will certainly improve the development of lipid-based transfection reagents in therapy and drug delivery with higher efficiency and lower side effects, a long-term goal in medical and biotechnological fields (90).

Direct observation of LUVs and GUVs enables the measurement of a number of mechanical properties (i.e. tension, curvature, elasticity) or molecular parameters (i.e. diffusion coefficient, lipid order) that are modified during the evolution of fusion and its intermediates. We envisage that our approach could be easily adapted to the study of fusion with SNARE-reconstituted vesicles in the presence of accessory proteins, and thus resolve how accessory proteins or other fusogens influence each intermediate independently. Single GUV observation and manipulation have the additional advantage that these properties can be measured or changed in real time for the very same vesicle, an approach that is not possible with any other fusion assay.

Supporting Material

Materials and methods; data on lipid transfer; microfluidic device experiment; details and data for intensity-based FRET and FLIM-FRET; quenching and FRAP experiments; movies.

Author Contributions

The manuscript was written through contributions of all authors. All authors have given approval to the final version of the manuscript.

Acknowledgements

This work is part of the MaxSynBio consortium which was jointly funded by the Federal Ministry of Education and Research of Germany and the Max Planck Society. The financial support of Fapesp is

acknowledged (process numbers 11/22171-6, 13/07246-5 and 16/13368-4). We thank J. Steinkühler for the help in designing the intensity FRET assay.

References

1. Martens, S., and H. T. McMahon. 2008. Mechanisms of membrane fusion: disparate players and common principles. Nat Rev Mol Cell Biol 9:543-556.
2. Jahn, R., T. Lang, and T. C. Sudhof. 2003. Membrane fusion. Cell 112:519-533.
3. Chernomordik, L. V., and M. M. Kozlov. 2008. Mechanics of membrane fusion. Nat. Struct. Mol. Biol. 15:675-683.
4. Jahn, R., and R. H. Scheller. 2006. SNAREs - engines for membrane fusion. Nat. Rev. Mol. Cell Biol. 7:631-643.
5. Wickner, W., and R. Schekman. 2008. Membrane fusion. Nat Struct Mol Biol 15:658-664.
6. Gong, B., B.-K. Choi, J.-Y. Kim, D. Shetty, Y. H. Ko, N. Selvapalam, N. K. Lee, and K. Kim. 2015. High Affinity Host–Guest FRET Pair for Single-Vesicle Content-Mixing Assay: Observation of Flickering Fusion Events. J. Am. Chem. Soc. 137:8908-8911.
7. Marsden, H. R., I. Tomatsu, and A. Kros. 2011. Model systems for membrane fusion. Chem. Soc. Rev. 40:1572-1585.
8. Lu, X., F. Zhang, J. A. McNew, and Y.-K. Shin. 2005. Membrane Fusion Induced by Neuronal SNAREs Transits through Hemifusion. J. Biol. Chem. 280:30538-30541.
9. Kim, J.-Y., B.-K. Choi, M.-G. Choi, S.-A. Kim, Y. Lai, Y.-K. Shin, and N. K. Lee. 2012. Solution single-vesicle assay reveals PIP(2)-mediated sequential actions of synaptotagmin-1 on SNAREs. The EMBO Journal 31:2144-2155.
10. Haluska, C. K., K. A. Riske, V. Marchi-Artzner, J. M. Lehn, R. Lipowsky, and R. Dimova. 2006. Time scales of membrane fusion revealed by direct imaging of vesicle fusion with high temporal resolution. Proc. Natl. Acad. Sci. U. S. A. 103:15841-15846.
11. Yang, P., R. Lipowsky, and R. Dimova. 2009. Nanoparticle Formation in Giant Vesicles: Synthesis in Biomimetic Compartments. Small 5:2033-2037.
12. Steubing, R. W., S. Cheng, W. H. Wright, Y. Numajiri, and M. W. Berns. 1991. Laser induced cell fusion in combination with optical tweezers: The laser cell fusion trap. Cytometry 12:505-510.
13. Bahadori, A., L. B. Oddershede, and P. M. Bendix. 2017. Hot-nanoparticle-mediated fusion of selected cells. Nano Research 10:2034-2045.
14. Bahadori, A., G. Moreno-Pescador, L. B. Oddershede, and P. M. Bendix. 2018. Remotely controlled fusion of selected vesicles and living cells: a key issue review. Rep. Prog. Phys. 81:032602.
15. Marsden, H. R., N. A. Elbers, P. H. H. Bomans, N. A. J. M. Sommerdijk, and A. Kros. 2009. A Reduced SNARE Model for Membrane Fusion. Angew. Chem. Int. Ed. 48:2330-2333.
16. Bao, C., G. Pähler, B. Geil, and A. Janshoff. 2013. Optical Fusion Assay Based on Membrane-Coated Spheres in a 2D Assembly. J. Am. Chem. Soc. 135:12176-12179.
17. Lentz, B. R. 2007. PEG as a tool to gain insight into membrane fusion. Eur. Biophys. J. 36:315-326.
18. Yaroslavov, A. A., A. V. Sybachin, E. Kesselman, J. Schmidt, Y. Talmon, S. A. A. Rizvi, and F. M. Menger. 2011. Liposome Fusion Rates Depend upon the Conformation of Polycation Catalysts. J. Am. Chem. Soc. 133:2881-2883.
19. Struck, D. K., D. Hoekstra, and R. E. Pagano. 1981. Use of Resonance Energy-Transfer to Monitor Membrane-Fusion. Biochemistry 20:4093-4099.
20. Loyter, A., V. Citovsky, and R. Blumenthal. 2006. The Use of Fluorescence Dequenching Measurements to Follow Viral Membrane Fusion Events. In Methods Biochem. Anal.

21. Martens, S., M. M. Kozlov, and H. T. McMahon. 2007. How synaptotagmin promotes membrane fusion. Science 316:1205-1208.
22. Chan, Y. H. M., B. van Lengerich, and S. G. Boxer. 2009. Effects of linker sequences on vesicle fusion mediated by lipid-anchored DNA oligonucleotides. Proc. Natl. Acad. Sci. U. S. A. 106:979-984.
23. McNew, J. A., F. Parlati, R. Fukuda, R. J. Johnston, K. Paz, F. Paumet, T. H. Sollner, and J. E. Rothman. 2000. Compartmental specificity of cellular membrane fusion encoded in SNARE proteins. Nature 407:153-159.
24. Karatekin, E., J. Di Giovanni, C. Iborra, J. Coleman, B. O'Shaughnessy, M. Seagar, and J. E. Rothman. 2010. A fast, single-vesicle fusion assay mimics physiological SNARE requirements. Proc. Natl. Acad. Sci. U. S. A. 107:3517-3521.
25. Cypionka, A., A. Stein, J. M. Hernandez, H. Hippchen, R. Jahn, and P. J. Walla. 2009. Discrimination between docking and fusion of liposomes reconstituted with neuronal SNARE-proteins using FCS. Proc. Natl. Acad. Sci. U. S. A. 106:18575-18580.
26. Witkowska, A., and R. Jahn. 2017. Rapid SNARE-Mediated Fusion of Liposomes and Chromaffin Granules with Giant Unilamellar Vesicles. Biophys. J. 113:1251-1259.
27. Kuhlmann, J. W., M. Junius, U. Diederichsen, and C. Steinem. 2017. SNARE-Mediated Single-Vesicle Fusion Events with Supported and Freestanding Lipid Membranes. Biophys. J. 112:2348-2356.
28. Lou, X., J. Kim, B. J. Hawk, and Y.-K. Shin. 2017. α-Synuclein may cross-bridge v-SNARE and acidic phospholipids to facilitate SNARE-dependent vesicle docking. Biochem. J. 474:2039-2049.
29. Dimova, R., S. Aranda, N. Bezlyepkina, V. Nikolov, K. A. Riske, and R. Lipowsky. 2006. A practical guide to giant vesicles. Probing the membrane nanoregime via optical microscopy. J. Phys.: Condens. Matter 18:S1151-S1176.
30. Kahya, N., E. I. Pecheur, W. P. de Boeij, D. A. Wiersma, and D. Hoekstra. 2001. Reconstitution of membrane proteins into giant unilamellar vesicles via peptide-induced fusion. Biophys. J. 81:1464-1474.
31. Nikolaus, J., M. Stöckl, D. Langosch, R. Volkmer, and A. Herrmann. 2010. Direct Visualization of Large and Protein-Free Hemifusion Diaphragms. Biophys. J. 98:1192-1199.
32. Rørvig-Lund, A., A. Bahadori, S. Semsey, P. M. Bendix, and L. B. Oddershede. 2015. Vesicle Fusion Triggered by Optically Heated Gold Nanoparticles. Nano Lett. 15:4183-4188.
33. Riske, K. A., N. Bezlyepkina, R. Lipowsky, and R. Dimova. 2006. Electrofusion of model lipid membranes viewed with high temporal resolution. Biophys. Rev. Lett. 1:387-400.
34. Tareste, D., J. Shen, T. J. Melia, and J. E. Rothman. 2008. SNAREpin/Munc18 promotes adhesion and fusion of large vesicles to giant membranes. Proc. Natl. Acad. Sci. U. S. A. 105:2380-2385.
35. Lei, G. H., and R. C. MacDonald. 2003. Lipid bilayer vesicle fusion: Intermediates captured by high-speed microfluorescence spectroscopy. Biophys. J. 85:1585-1599.
36. Tanaka, T., and M. Yamazaki. 2004. Membrane Fusion of Giant Unilamellar Vesicles of Neutral Phospholipid Membranes Induced by La3+. Langmuir 20:5160-5164.
37. Kliesch, T.-T., J. Dietz, L. Turco, P. Halder, E. Polo, M. Tarantola, R. Jahn, and A. Janshoff. 2017. Membrane tension increases fusion efficiency of model membranes in the presence of SNAREs. Sci Rep 7:12070.
38. Trier, S., J. R. Henriksen, and T. L. Andresen. 2011. Membrane fusion of pH-sensitive liposomes - a quantitative study using giant unilamellar vesicles. Soft Matter 7:9027-9034.
39. Csiszar, A., N. Hersch, S. Dieluweit, R. Biehl, R. Merkel, and B. Hoffmann. 2010. Novel Fusogenic Liposomes for Fluorescent Cell Labeling and Membrane Modification. Bioconjug. Chem. 21:537-543.
40. Kleusch, C., N. Hersch, B. Hoffmann, R. Merkel, and A. Csiszar. 2012. Fluorescent Lipids: Functional Parts of Fusogenic Liposomes and Tools for Cell Membrane Labeling and Visualization. Molecules 17:1055-1073.

41. Lira, R. B., M. A. B. L. Seabra, A. L. L. Matos, J. V. Vasconcelos, D. P. Bezerra, E. de Paula, B. S. Santos, and A. Fontes. 2013. Studies on intracellular delivery of carboxyl-coated CdTe quantum dots mediated by fusogenic liposomes. J Mater Chem B 1:4297-4305.
42. Kube, S., N. Hersch, E. Naumovska, T. Gensch, J. Hendriks, A. Franzen, L. Landvogt, J.-P. Siebrasse, U. Kubitscheck, B. Hoffmann, R. Merkel, and A. Csiszár. 2017. Fusogenic Liposomes as Nanocarriers for the Delivery of Intracellular Proteins. Langmuir 33:1051-1059.
43. Lira, R. B., J. Steinkuhler, R. L. Knorr, R. Dimova, and K. A. Riske. 2016. Posing for a picture: vesicle immobilization in agarose gel. Sci Rep 6:25254.
44. Steinkühler, J., P. De Tillieux, R. L. Knorr, R. Lipowsky, and R. Dimova. 2018. Charged giant unilamellar vesicles prepared by electroformation exhibit nanotubes and transbilayer lipid asymmetry. Sci Rep 8:11838.
45. Weinberger, A., F. C. Tsai, G. H. Koenderink, T. F. Schmidt, R. Itri, W. Meier, T. Schmatko, A. Schroder, and C. Marques. 2013. Gel-Assisted Formation of Giant Unilamellar Vesicles. Biophys. J. 105:154-164.
46. Riske, K. A., and R. Dimova. 2005. Electro-deformation and poration of giant vesicles viewed with high temporal resolution. Biophys. J. 88:1143-1155.
47. Agudo-Canalejo, J., and R. Lipowsky. 2015. Critical Particle Sizes for the Engulfment of Nanoparticles by Membranes and Vesicles with Bilayer Asymmetry. Acs Nano 9:3704-3720.
48. Robinson, T., P. Kuhn, K. Eyer, and P. S. Dittrich. 2013. Microfluidic trapping of giant unilamellar vesicles to study transport through a membrane pore. Biomicrofluidics 7.
49. Robinson, T., P. E. Verboket, K. Eyer, and P. S. Dittrich. 2014. Controllable electrofusion of lipid vesicles: initiation and analysis of reactions within biomimetic containers. Lab Chip 14:2852-2859.
50. Skelley, A. M., O. Kirak, H. Suh, R. Jaenisch, and J. Voldman. 2009. Microfluidic control of cell pairing and fusion. Nat. Methods 6:147.
51. Yoon, T. Y., B. Okumus, F. Zhang, Y. K. Shin, and T. Ha. 2006. Multiple intermediates in SNARE-induced membrane fusion. Proc. Natl. Acad. Sci. U. S. A. 103:19731-19736.
52. Mattei, B., R. B. Lira, K. R. Perez, and K. A. Riske. 2017. Membrane permeabilization induced by Triton X-100: The role of membrane phase state and edge tension. Chem. Phys. Lipids 202:28-37.
53. Aranda, S., K. A. Riske, R. Lipowsky, and R. Dimova. 2008. Morphological transitions of vesicles induced by alternating electric fields. Biophys. J. 95:L19-L21.
54. Dimova, R., K. A. Riske, S. Aranda, N. Bezlyepkina, R. L. Knorr, and R. Lipowsky. 2007. Giant vesicles in electric fields. Soft Matter 3:817-827.
55. Riske, K. A., T. P. Sudbrack, N. L. Archilha, A. F. Uchoa, A. P. Schroder, C. M. Marques, M. S. Baptista, and R. Itri. 2009. Giant Vesicles under Oxidative Stress Induced by a Membrane-Anchored Photosensitizer. Biophys. J. 97:1362-1370.
56. Mattei, B., A. D. C. Franca, and K. A. Riske. 2015. Solubilization of Binary Lipid Mixtures by the Detergent Triton X-100: The Role of Cholesterol. Langmuir 31:378-386.
57. Dimova, R., N. Bezlyepkina, M. D. Jordo, R. L. Knorr, K. A. Riske, M. Staykova, P. M. Vlahovska, T. Yamamoto, P. Yang, and R. Lipowsky. 2009. Vesicles in electric fields: Some novel aspects of membrane behavior. Soft Matter 5:3201-3212.
58. Wong, J. L., D. E. Koppel, A. E. Cowan, and G. M. Wessel. 2007. Membrane hemifusion is a stable intermediate of exocytosis. Dev. Cell 12:653-659.
59. White, J. M., and J. D. Castle. 2005. Searching for the silver lining. Nat. Struct. Mol. Biol. 12:382-384.
60. McIntyre, J. C., and R. G. Sleight. 1991. Fluorescence Assay for Phospholipid Membrane Asymmetry. Biochemistry 30:11819-11827.

61. Moreno, M. J., L. M. B. B. Estronca, and W. L. C. Vaz. 2006. Translocation of Phospholipids and Dithionite Permeability in Liquid-Ordered and Liquid-Disordered Membranes. Biophys. J. 91:873-881.
62. Bezlyepkina, N., R. S. Gracià, P. Shchelokovskyy, R. Lipowsky, and R. Dimova. 2013. Phase Diagram and Tie-Line Determination for the Ternary Mixture DOPC/eSM/Cholesterol. Biophys. J. 104:1456-1464.
63. Stamatatos, L., R. Leventis, M. J. Zuckermann, and J. R. Silvius. 1988. Interactions of Cationic Lipid Vesicles with Negatively Charged Phospholipid-Vesicles and Biological-Membranes. Biochemistry 27:3917-3925.
64. Islam, M. Z., H. Ariyama, J. M. Alam, and M. Yamazaki. 2014. Entry of Cell-Penetrating Peptide Transportan 10 into a Single Vesicle by Translocating Across Lipid Membrane and Its Induced Pores. Biochemistry 53:386-396.
65. Biner, O., T. Schick, Y. Muller, and C. von Ballmoos. 2016. Delivery of membrane proteins into small and giant unilamellar vesicles by charge-mediated fusion. FEBS Lett. 590:2051-2062.
66. Lakowicz, J. R. 2006. Principles of fluorescence spectroscopy. Springer, New York.
67. Li, Y., R. Lipowsky, and R. Dimova. 2011. Membrane nanotubes induced by aqueous phase separation and stabilized by spontaneous curvature. Proc. Natl. Acad. Sci. U. S. A. 108:4731-4736.
68. Bassereau, P., R. Jin, T. Baumgart, M. Deserno, R. Dimova, V. A. Frolov, P. V. Bashkirov, H. Grubmüller, R. Jahn, H. J. Risselada, L. Johannes, M. M. Kozlov, R. Lipowsky, T. J. Pucadyil, W. F. Zeno, J. C. Stachowiak, D. Stamou, A. Breuer, L. Lauritsen, C. Simon, C. Sykes, G. A. Voth, and T. R. Weikl. 2018. The 2018 Biomembrane Curvature and Remodeling Roadmap. Journal of Physics D-Applied Physics 51:343001.
69. Lipowsky, R. 2013. Spontaneous tubulation of membranes and vesicles reveals membrane tension generated by spontaneous curvature. Faraday Discuss. 161:305-331.
70. Dasgupta, R., M. S. Miettinen, N. Fricke, R. Lipowsky, and R. Dimova. 2018. The glycolipid GM1 reshapes asymmetric biomembranes and giant vesicles by curvature generation. Proc. Natl. Acad. Sci. U. S. A. 115:5756–5761.
71. Solon, J., J. Pecreaux, P. Girard, M. C. Faure, J. Prost, and P. Bassereau. 2006. Negative tension induced by lipid uptake. Phys. Rev. Lett. 97:098103.
72. Georgiev, V. N., A. Grafmüller, D. Bléger, S. Hecht, S. Kunstmann, S. Barbirz, R. Lipowsky, and R. Dimova. 2018. Area Increase and Budding in Giant Vesicles Triggered by Light: Behind the Scene. Advanced Science:1800432.
73. Mertins, O., and R. Dimova. 2013. Insights on the Interactions of Chitosan with Phospholipid Vesicles. Part II: Membrane Stiffening and Pore Formation. Langmuir 29:14552-14559.
74. Fricke, N., and R. Dimova. 2016. GM1 Softens POPC Membranes and Induces the Formation of Micron-Sized Domains. Biophys. J. 111:1935-1945.
75. Bhatia, T., J. Agudo-Canalejo, R. Dimova, and R. Lipowsky. 2018. Membrane Nanotubes Increase the Robustness of Giant Vesicles. Acs Nano 12:4478-4485.
76. Weber, T., B. V. Zemelman, J. A. McNew, B. Westermann, M. Gmachl, F. Parlati, T. H. Sollner, and J. E. Rothman. 1998. SNAREpins: Minimal machinery for membrane fusion. Cell 92:759-772.
77. Kyoung, M., A. Srivastava, Y. X. Zhang, J. J. Diao, M. Vrljic, P. Grob, E. Nogales, S. Chu, and A. T. Brunger. 2011. In vitro system capable of differentiating fast Ca2+-triggered content mixing from lipid exchange for mechanistic studies of neurotransmitter release. Proc. Natl. Acad. Sci. U. S. A. 108:E304-E313.
78. Nickel, W., T. Weber, J. A. McNew, F. Parlati, T. H. Sollner, and J. E. Rothman. 1999. Content mixing and membrane integrity during membrane fusion driven by pairing of isolated v-SNAREs and t-SNAREs. Proc. Natl. Acad. Sci. U. S. A. 96:12571-12576.

79. Starai, V. J., Y. Jun, and W. Wickner. 2007. Excess vacuolar SNAREs drive lysis and Rab bypass fusion. Proceedings of the National Academy of Sciences 104:13551.
80. Engel, A., and P. Walter. 2008. Membrane lysis during biological membrane fusion: collateral damage by misregulated fusion machines. The Journal of Cell Biology 183:181-186.
81. Smith, Elizabeth A., and James C. Weisshaar. 2011. Docking, Not Fusion, as the Rate-Limiting Step in a SNARE-Driven Vesicle Fusion Assay. Biophys. J. 100:2141-2150.
82. van Lengerich, B., Robert J. Rawle, Poul M. Bendix, and Steven G. Boxer. 2013. Individual Vesicle Fusion Events Mediated by Lipid-Anchored DNA. Biophys. J. 105:409-419.
83. Simonsson, L., P. Jönsson, G. Stengel, and F. Höök. 2010. Site-Specific DNA-Controlled Fusion of Single Lipid Vesicles to Supported Lipid Bilayers. Chemphyschem 11:1011-1017.
84. Rawle, Robert J., B. van Lengerich, M. Chung, Poul M. Bendix, and Steven G. Boxer. 2011. Vesicle Fusion Observed by Content Transfer across a Tethered Lipid Bilayer. Biophys. J. 101:L37-L39.
85. Yu, M., R. B. Lira, K. A. Riske, R. Dimova, and H. Lin. 2015. Ellipsoidal Relaxation of Deformed Vesicles. Phys. Rev. Lett. 115:128303.
86. Shillcock, J. C., and R. Lipowsky. 2005. Tension-induced fusion of bilayer membranes and vesicles. Nat. Mater. 4:225-228.
87. Kozlov, M. M., and L. V. Chernomordik. 2015. Membrane tension and membrane fusion. Curr. Opin. Struct. Biol. 33:61-67.
88. Koltover, I., T. Salditt, J. O. Radler, and C. R. Safinya. 1998. An inverted hexagonal phase of cationic liposome-DNA complexes related to DNA release and delivery. Science 281:78-81.
89. Lin, A. J., N. L. Slack, A. Ahmad, C. X. George, C. E. Samuel, and C. R. Safinya. 2003. Three-Dimensional Imaging of Lipid Gene-Carriers: Membrane Charge Density Controls Universal Transfection Behavior in Lamellar Cationic Liposome-DNA Complexes. Biophys. J. 84:3307-3316.
90. Ewert, K., A. Ahmad, H. M. Evans, and C. R. Safinya. 2005. Cationic lipid–DNA complexes for non-viral gene therapy: relating supramolecular structures to cellular pathways. Expert Opinion on Biological Therapy 5:33-53.